npj | climate and atmospheric science

Article

Published in partnership with CECCR at King Abdulaziz University

https://doi.org/10.1038/s41612-024-00770-7

Sea-ice loss in Eurasian Arctic coast intensifies heavy Meiyu-Baiu rainfall associated with Indian Ocean warming

Xiaodan Chen[1], Zhiping Wen[1,2,3] ✉, Jiping Liu[4], Wei Mei[1], Ruonan Zhang[1], Sihua Huang[1], Yuanyuan Guo[1] & Juncong Li[1,5]

Heavy Meiyu-Baiu rainfall can pose threat to the dense population in East Asia by catastrophic flooding. Although previous studies have identified Indian Ocean (IO) warming as the major cause of heavy Meiyu-Baiu rainfall, it failed to predict the record-breaking rainfall in July 2020. Synthesizing observational analysis, large-ensemble climate simulations, and atmospheric simulations, we show that sea-ice loss in the Kara Sea in May can intensify the IO warming-induced heavy Meiyu-Baiu rainfall and well explains the record-breaking rainfall in July 2020. In the precondition of IO warming, sea-ice loss tends to prolong Meiyu-Baiu season and strengthen convective activity over the Meiyu-Baiu region, thereby enhancing the IO warming-induced heavy Meiyu-Baiu rainfall by ~50% and doubling the risk of extreme events comparable to or greater than the one in 2020. A statistical model is further constructed to demonstrate that taking Arctic sea ice into consideration can significantly improve the seasonal prediction of extreme Meiyu-Baiu rainfall.

In early summer, the East Asian summer monsoon marches northward into the subtropics and encounters relatively cold air camping at mid-to-high latitudes. This results in a quasi-stationary rain belt that typically starts in June and continues into July, known as Meiyu in China, Changma in Korea, and Baiu in Japan. Extreme Meiyu-Baiu rainfall along with excessive rainfall accumulation (such as those in 1998 and 2020) can cause disastrous floods and severe damage to lives and properties and thereby greatly impact the densely populated area extending from central-eastern China to Japan[1–3]. For instance, the extremely heavy Meiyu-Baiu rainfall in 2020 resulted in a massive economic loss of over 170 billion Chinese Yuan in China[4] and at least 40 deaths in southern Japan and forced hundreds of thousands of people to evacuate[5]. Therefore, a good understanding and accurate prediction of extreme Meiyu-Baiu rainfall is urgently needed[3,6,7].

Conventionally, heavy Meiyu-Baiu rainfall is linked to El Niño in the preceding winter and the associated Indian Ocean (IO) warming that often emerges in spring and persists into summer[6,8–11]. IO warming can generate an anomalous anticyclone over the Indo-Northwest Pacific, enhancing moisture supply and ascending motions over the Meiyu-Baiu region via strengthened low-level southwesterlies. However, when the prediction of Meiyu-Baiu rainfall relies primarily on low-latitude SST anomalies, the skill is still low in some cases. For example, IO warming in spring 2020 is a good predictor for the enhanced precipitation in June but not in July[11–14]. Thus, it is imperative to identify other key factors responsible for extremely heavy Meiyu-Baiu rainfall, especially those may act synergistically with the well-knowns in the tropics.

Rapid Arctic sea-ice loss and associated amplified warming in response to global climate change in recent decades have been shown to exert profound influences on mid- and high-latitude atmospheric circulation[15,16]. Arctic sea ice state may accordingly serve as a potential predictor for the East Asian summer rainfall[17–21]. Indeed, recent observational studies suggest that the loss of sea ice along the Siberian coast in early summer of 2020 might have contributed to the heavy Meiyu-Baiu rainfall by the warming and high-pressure anomalies over the East Siberia[22–24]. However, the relationship between Arctic sea ice and East Asian summer rainfall is not stationary over time[21] and varies greatly among studies[25], partly owing to the short record of reliable observations. It remains to determine the connections between the two and the underlying physical mechanisms. Here, we propose that Arctic sea ice can only significantly influence East Asian summer rainfall in conjunction with the Indian Ocean SST conditions. This is motivated by our recent finding that the simulated extreme Meiyu-Baiu rainfall in 2020 in an atmospheric model driven by observed IO SST anomalies can be

[1]Department of Atmospheric and Oceanic Sciences & Institute of Atmospheric Sciences, Fudan University, Shanghai, China. [2]Innovation Center of Ocean and Atmosphere System, Zhuhai Fudan Innovation Research Institute, Zhuhai, China. [3]Jiangsu Collaborative Innovation Center for Climate Change, Nanjing, China. [4]Sun Yat-Sen University, School of Atmospheric Sciences, Zhuhai, China. [5]Geophysical Institute, University of Bergen and Bjerknes Centre for Climate Research, Bergen, Norway. ✉e-mail: zpwen@fudan.edu.cn

significantly improved when observed Arctic sea-ice concentration (SIC) anomalies are also prescribed[26].

Because the concurrence of reduced Arctic sea ice and warm IO is rare in observations[26], in this study we take advantage of a set of large-ensemble climate simulations to test our hypothesis and explore the synergistic effect of Arctic sea ice and IO SST on extremely heavy Meiyu-Baiu rainfall. The simulations in use are a 100-member large ensemble of historical simulations by the Community Earth System Model v2 (CESM2)[27], referred to as CESM2LE (see Methods). The CESM2LE faithfully simulates the spatial and temporal characteristics of observed Meiyu-Baiu rainfall (Figs. S1 and S2 and Supplementary Notes). To focus on the variations and relationships within the climate system, the CESM2LE ensemble mean, which represents the forced signal, is removed from the 100 individual runs (see Methods for details). The rationale is that Arctic sea ice and IO SST are highly sensitive to climate change and the effects of external forcing may obscure the results.

Results

Simulated Sea-ice loss and Indian Ocean warming

After removing the forced warming signal in IO SST (dashed curve in Fig. S3a) from individual CESM2LE runs (gray solid curves in Fig. S3a), a simulation year with May IO SST outside of the ± 1 standard deviation (std) range is referred to as a warm IO (WIO) case or cold IO (CIO) case (Fig. S3b). In WIO cases, IO warming persists from spring to summer (Figs. S3c, d and S4b), typically following eastern Pacific (EP) warming in the preceding winter (Fig. S4a); this is consistent with the observed interaction between the tropical Pacific and Indian Oceans[10].

From spring to summer, the sea-ice melting expands eastward from the Barents Sea to the East Siberian Sea in both observations and CESM2LE simulations (Fig. S5a, b). The sea-ice loss in the Kara Sea (KS) in May generally predicts sea-ice loss along the Siberian coast earlier than usual (Fig. S5e, f), which represents a retreat of sea ice from the Eurasian Arctic coast. The KS sea ice extent (SIE) anomalies prior to May show a much lower predictive skill for the early-summer SIE along the Siberian coast (Fig. S6), likely due to the spring barrier of sea-ice prediction[28]. After removing the forced SIE decline (dashed curve in Fig. S5c) from individual CESM2LE runs (gray solid curves in Fig. S5c), we categorized simulation years with the May KS SIE outside of the ± 1 std range as high SIE (HSI) cases and low SIE (LSI) cases, respectively (Fig. S5d).

Years with WIO cases and LSI cases are referred to as WIO-LSI cases, while the remaining WIO cases and LSI cases are defined as WIO-noLSI cases and LSI-noWIO cases, respectively. Likewise, CIO-HSI and CIO-noHSI are short for the CIO cases with and without HSI cases, respectively. Consistent with the rare concurrence of significant IO warming and KS SIE loss in late spring-early summer in observations[26]. The KS SIE and IO SST in May are not significantly correlated in individual CESM2 simulations [r = -0.14 ± 0.13 (mean ± std)]. In the observation, the correlation coefficient of linearly detrended KS SIE and IO SST in May is as low as 0.11 (p = 0.39), although the correlation between their non-detrended timeseries is significant (r = -0.47, p < 0.01) that primarily represents the forced response to global warming. On the other hand, while the interannual variability of wintertime Barents-Kara sea ice is partially influenced by the concurrent El Niño–Southern Oscillation (ENSO)[29], the KS SIE in May does not show a significant correlation to the Niño3.4 index in the preceding winter (Methods) in the individual CESM2LE simulations (r = 0.06 ± 0.12) and observation from 1950-2014 (r = 0.03, p = 0.81). We thus conclude that the KS SIE in May is generally independent of the interannual variability in the tropical Indian and Pacific Oceans, justifying our claim that the KS SIE in May can potentially serve as an independent predictor for the Meiyu-Baiu rainfall.

Enhanced Meiyu-Baiu rainfall due to Arctic Sea-ice loss

Figure 1 displays the simulated precipitation anomalies during the Meiyu-Baiu season (i.e., averaged over June-July) in the WIO, WIO-LSI, and WIO-noLSI cases, respectively. As expected, precipitation is intensified over the

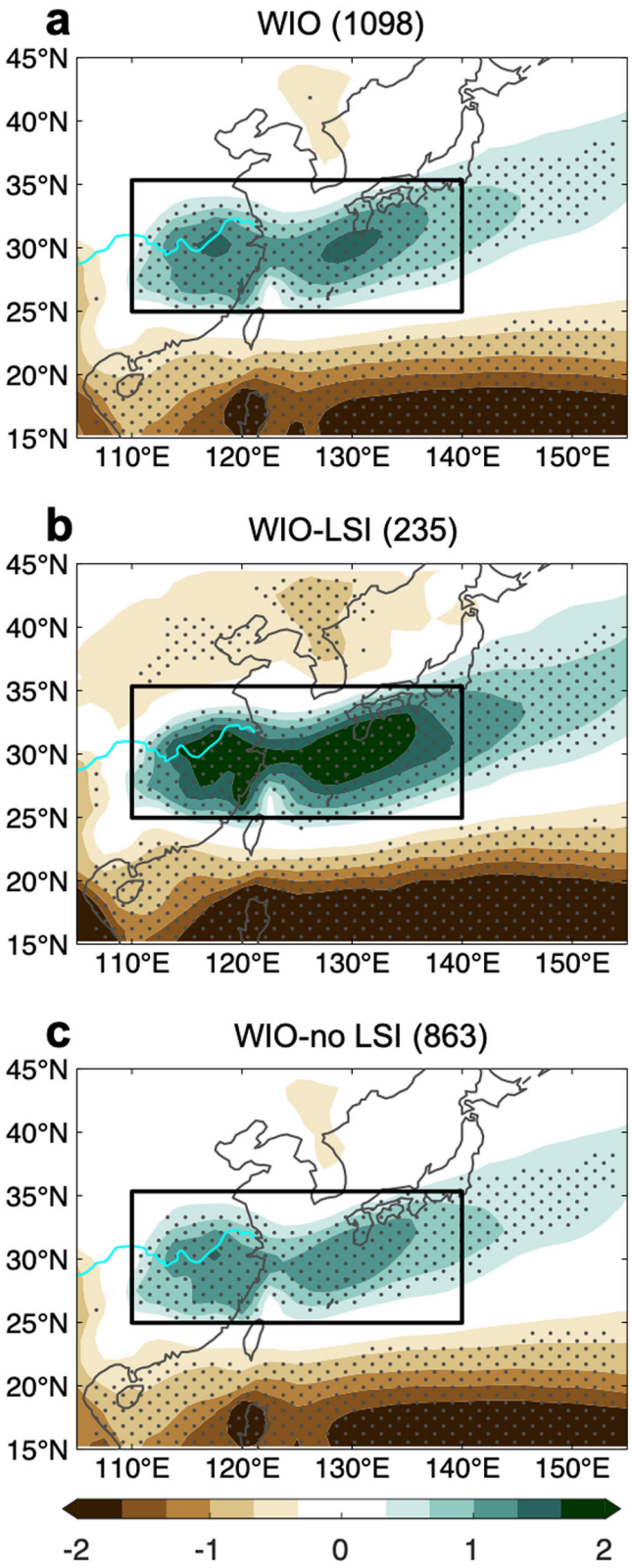

Fig. 1 | Meiyu-Baiu rainfall in WIO cases, WIO-LSI cases, and WIO-noLSI cases. Composite maps of CESM2LE-simulated precipitation anomalies [unit: mm/day] averaged from June to July for (**a**) WIO, (**b**) WIO-LSI, and (**c**) WIO-noLSI cases. The case number is shown in the parentheses. The stippling indicates statistical significance at the 5% level. Hereafter, the Meiyu-Baiu region is outlined by the black box (110°–140°E, 25°–35°N), and the Yangtze River is shown by the cyan line. The anomalies indicate deviations from 1981 to 2010 mean.

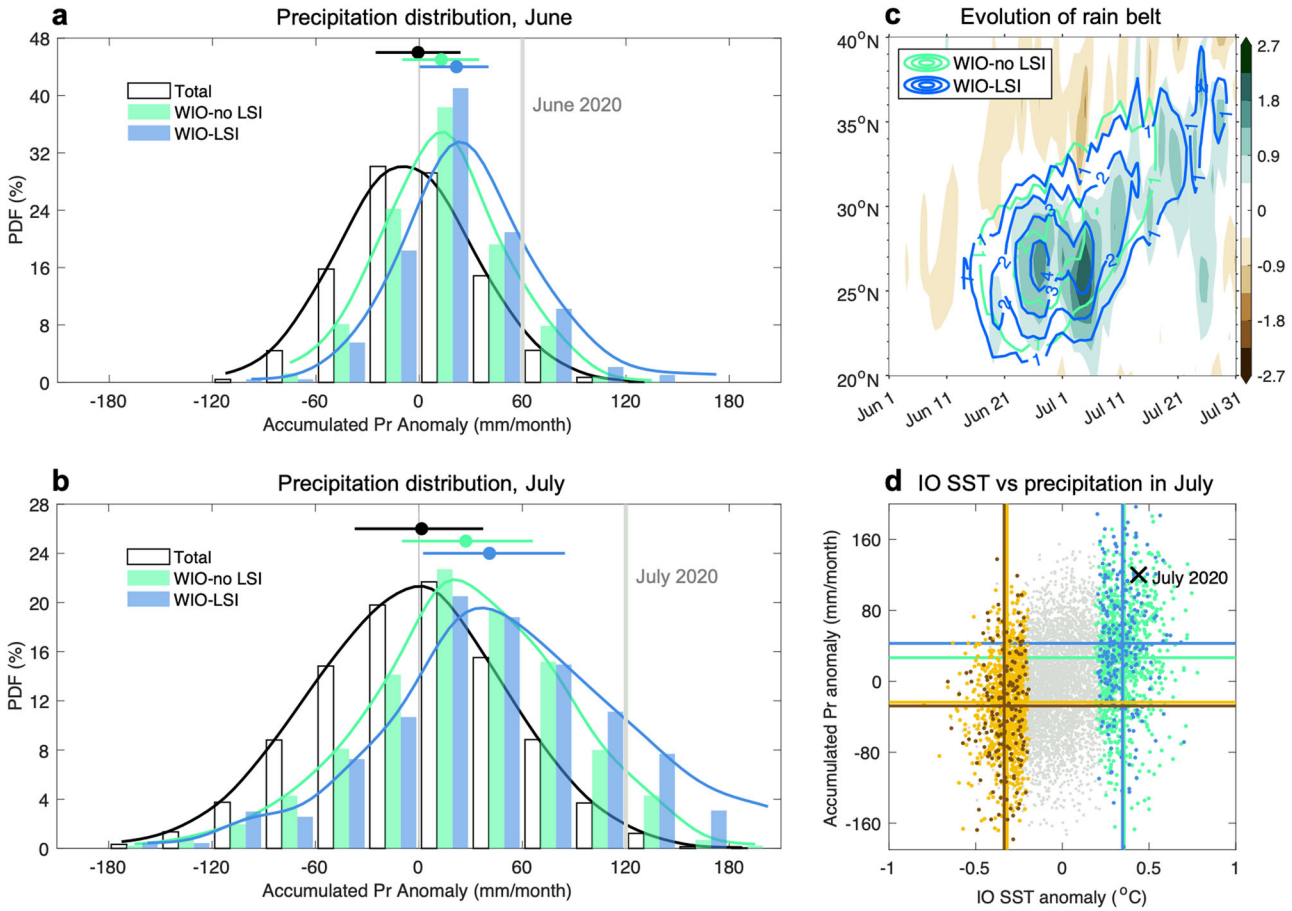

Fig. 2 | Contrast of Meiyu-Baiu rainfall between WIO-LSI and WIO-noLSI cases. Histograms (bars) and fitted distribution (curves) of CESM2LE-simulated precipitation anomalies accumulated during (**a**) June and (**b**) July over the Meiyu-Baiu region for all the simulation years (6500 years from 100 runs; white bars and black curve), WIO-noLSI (green) and WIO-LSI cases (blue). The medians and 25th to 75th percentile ranges are shown by dots and horizontal lines in corresponding colors. Gray lines indicate the observational results for June and July 2020 in ERA5. **c** CESM2LE-simulated daily precipitation anomalies averaged over 110°-140°E [contours interval = 2 mm/day; negative values are omitted] for WIO-noLSI (green) and WIO-LSI cases (blue) from June 1st to July 31st, with shadings showing their differences. **d** Scatter diagram of precipitation anomalies accumulated during July over the Meiyu-Baiu region as a function of IO sea surface temperature (SST) anomalies in May for individual CESM2LE runs (gray dots). Results for WIO-LSI (blue), WIO-no LSI (green), CIO-HSI (brown), and CIO-noHSI (yellow) cases are highlighted by different colors, with vertical and horizontal lines in corresponding colors indicating the averages. The black cross indicates the observations of July 2020.

Meiyu-Baiu region in the WIO cases (Fig. 1a), caused by the strengthened southwesterlies on the western flank of the anomalous anticyclone over the Northwest Pacific[10,30]. What is intriguing is that the IO warming-induced heavy rainfall is greatly enhanced when low SIE coexists in May (Fig. 1b). The distinct contrast of Meiyu-Baiu rainfall between the WIO-LSI cases and WIO-noLSI cases (cf. Fig. 1b, c) indicates that the low SIE may contribute to heavy Meiyu-Baiu rainfall. An examination of LSI-noWIO cases suggests that low KS SIE in May alone is insufficient to promote Meiyu-Baiu rainfall, as the LSI-noWIO cases exhibit minimal precipitation anomalies over the Meiyu-Baiu region (Fig. S7b), in stark contrast to the pronounced precipitation difference between WIO-LSI and WIO-noLSI cases (Fig. S7c).

To quantify the influence of low SIE on the heavy rainfall induced by IO warming, we examined the distribution of precipitation anomalies averaged over the Meiyu-Baiu region for the WIO-LSI and WIO-noLSI cases and compared them with that for all simulation years (Fig. 2a, b). In comparison with the WIO-noLSI cases (green histograms and curves), the distribution for the WIO-LSI cases obviously shifts rightward in both June and July (blue histograms and curves). The relay of heavy rainfall from June to July dramatically increases the risk of flash floods when rivers reach alerting levels and saturated soil cannot absorb any more water, which is a common cause of catastrophic Meiyu-Baiu cases[14,31]. Moreover, the distribution for the WIO-LSI cases shows a heavier right tail compared with that for the WIO-noLSI cases (Fig. 2a, b), suggesting an increased risk of extremely heavy Meiyu-Baiu rainfall. The likelihood of extremely heavy rainfall cases comparable to or more severe than the 2020 cases (highlighted by gray vertical lines in Fig. 2a, b) in the WIO-LSI cases is doubled in comparison with that in the WIO-noLSI cases, increasing from ~7% to ~13% in June and from ~5% to ~11% in July.

The distribution change is more evident in July (Fig. 2b) than in June (Fig. 2a). In July, the median of the precipitation anomalies in the WIO-LSI cases is ~45 mm (difference between blue and black dots in Fig. 2b), which is ~50% greater than that in the WIO-noLSI cases (difference between green and black dots in Fig. 2b). The median of the precipitation anomalies in June is also ~45% higher in the WIO-LSI cases (Fig. 2a). However, the precipitation anomalies in June are relatively small, accounting for only 27% of the June-July mean changes. This is probably due to the smaller year-to-year variations in June than in July (cf. Fig. S2c, d) and the lagged response of atmosphere circulation to Arctic sea-ice loss[32,33]. Examination of daily evolution of the Meiyu-Baiu rain belt averaged between 110° and 140°E (Fig. 2c) shows that, compared to the climatological northward-moving rain belt (Fig. S1c), WIO-noLSI cases exhibit positive anomalies from late June to mid-July (green contours in Fig. 2c), while WIO-LSI cases show positive anomalies from late June through the entire July (blue contours in Fig. 2c). Their difference occurs mainly from late-June through July and is modest

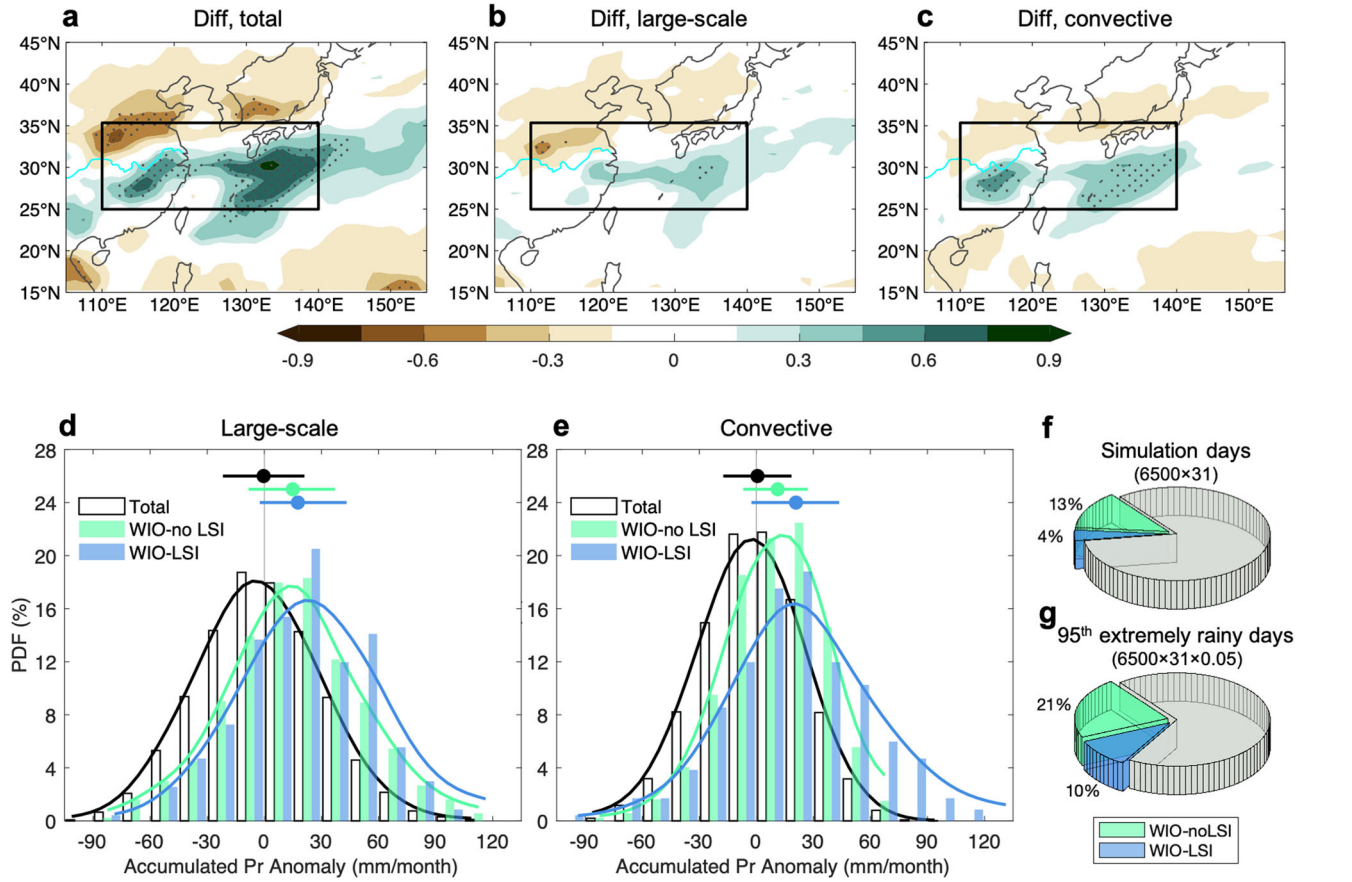

Fig. 3 | Differences in large-scale and convective precipitation. a Differences in CESM2LE-simulated precipitation anomalies [unit: mm/day] between WIO-LSI and WIO-noLSI cases in July, as well as the (**b**) large-scale and (**c**) convective components. **d**–**e** Similar to Fig. 2b, but for large-scale and convective components of the precipitation anomalies. **f**, **g** Partitions of July days occurring in WIO-LSI (blue) and WIO-noLSI cases (green) for (**f**) all the CESM2LE simulation days in July and (**g**) CESM2LE-simulated extremely heavy rainy days in July (see supplementary for the definition).

before late June (shadings in Fig. 2c). These results suggest that the Meiyu-Baiu season is prolonged in the WIO-LSI cases relative to that in the WIO-noLSI cases, with the onset date being barely affected. Since no discernible difference in the IO SST between the WIO-LSI and WIO-noLSI cases (green and blue vertical lines in Fig. 2d) can be found, the identified rainfall difference is unlikely caused by IO SSTs and their induced atmospheric responses. On the other hand, high SIE can exacerbate the insufficient Meiyu-Baiu rainfall caused by cold IO but with a much weaker magnitude (yellow and brown horizontal lines in Fig. 2d), indicating an asymmetry in the combined effect of KS SIE and IO SST on Meiyu-Baiu rainfall.

We further break down the precipitation differences between the WIO-LSI and WIO-noLSI cases in July (Fig. 3a) into two components: large-scale precipitation and convective precipitation (Fig. 3b, c). It appears that both the large-scale and convective components increase significantly over the ocean south of Japan (Fig. 3b, c), whereas only convective component shows significant increase around the middle-lower reaches of the Yangtze River in East China (Fig. 3c).

When averaged over the entire Meiyu-Baiu region, the difference in precipitation between the WIO-LSI and WIO-noLSI cases is mostly due to an increase in the convective component (compare blue and green dots in Fig. 3d, e). The convective component of precipitation averaged over the entire Meiyu-Baiu region increases by nearly 90% in the WIO-LSI cases compared with that in the WIO-noLSI cases (Fig. 3e), while the large-scale component shows only a slight increase (less than 10%; Fig. 3d). The substantial increase in convective precipitation suggests a risk of flash floods that are largely driven by high rainfall rates in convective storms.

Heavy precipitation occurring within a single day can be devastating when the volume of rainfall exceeds the infiltration rate of soil, which can result in rapid runoff, overflow, and urban waterlogging. As illustrated in Fig. 3f, g, approximately 10% of the extremely heavy rainy days during July in CESM2LE occur in the WIO-LSI cases (blue slice in Fig. 4g), although WIO-LSI cases only constitute about 4% of the total simulation days (blue slice in Fig. 4f). In contrast, days in the WIO-noLSI cases account for 21% of the extremely heavy rainy days (green slice in Fig. 4g) while constitute 13% of the total simulation days in July (green slice in Fig. 4f). More straightforward, nearly 13% of the July days in the WIO-LSI cases experience extremely heavy rainfall, while the proportion is just above 8% in the WIO-noLSI cases. The likelihood of extremely heavy rainy days in the WIO-LSI cases is 1.6 times that in the WIO-noLSI cases.

Underlying mechanisms

As described above, low KS SIE can enhance the heavy Meiyu-Baiu rainfall caused by IO warming, primarily by strengthening convective activity over the Meiyu-Baiu region in July. Next, we explore the possible physical processes that link the reduced sea ice to the enhanced convection over the Meiyu-Baiu region on the precondition of IO warming. Convective available potential energy (CAPE) is a crucial thermodynamic ingredient for deep convection and directly affects the frequency and intensity of convective precipitation. The increase in CAPE is greater in the WIO-LSI cases than in the WIO-noLSI cases (Fig. 4a, b). The spatial distribution of the difference resembles that of convective precipitation, with two local maximums over the sea south of Japan and around the middle-lower reaches of the Yangtze River, respectively (cf. Figs. 3c and 4c).

An increase in CAPE usually results from excessive low-level moisture and an increased lapse rate[34,35]. The air temperature difference between the WIO-LSI and WIO-noLSI cases shows that a remarkable cooling in the

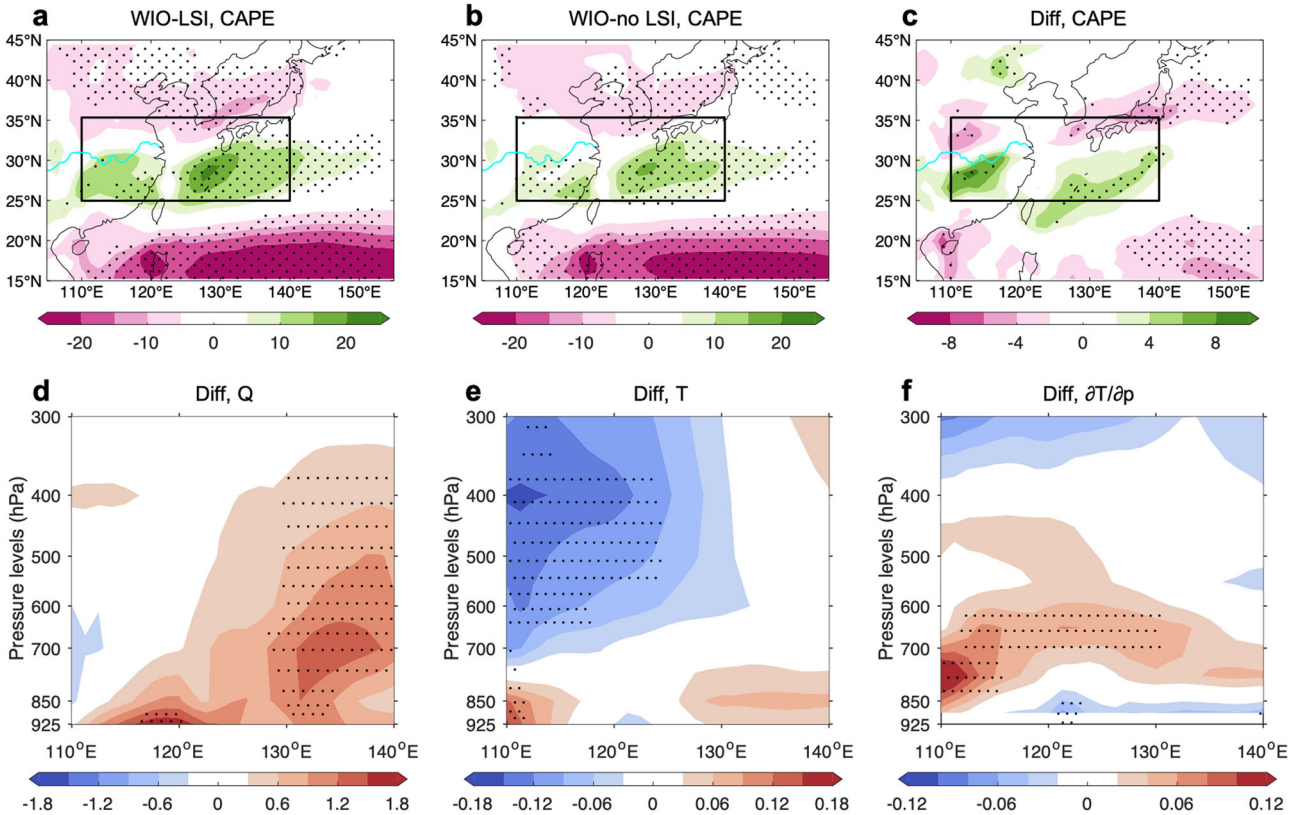

Fig. 4 | Differences in convective available potential energy (CAPE) and thermal conditions. CESM2LE-simulated CAPE anomalies [unit: J/kg] in July in (**a**) WIO-LSI and (**b**) WIO-noLSI cases and (**c**) their differences. Differences in CESM2LE-simulated (**d**) specific humidity [unit: 10^{-4}kg/kg], (**e**) air temperature [unit: °C], and (**f**) vertical differential of air temperature [unit: °C/hPa] averaged over 25°-35°N in July between WIO-LSI and WIO-noLSI cases. The stippling represents statistical significance at the 5% level.

mid-upper troposphere and moderate warming near the surface in the western Meiyu-Baiu region (Fig. 4e). The pronounced aloft cooling and moderate surface warming results in a steeper lapse rate in the lower troposphere in the western Meiyu-Baiu region (Fig. 4f), leading to a more unstable environment that favors convective overturning and thunderstorm[36], which is consistent with the increased CAPE (Fig. 4c) and convective precipitation (Fig. 3c) around the middle-lower reaches of the Yangtze River. The mid-upper tropospheric cooling in the western Meiyu-Baiu region also constrains moisture near the surface (Fig. 4d), lowering the lifting condensation level and increasing buoyancy. By contrast, in the eastern Meiyu-Baiu region, the change in temperature is rather modest (Fig. 4e), but specific humidity increases throughout the troposphere (Fig. 4d). Thus, the increase of convective activity over the middle-lower reaches of the Yangtze River is due to a combination of mid-upper tropospheric cooling and excessive near-surface moisture, whereas the strengthened convection over the sea south of Japan may be attributed to abundant moisture through the entire troposphere.

To understand how the low SIE strengthens the moisture convergence over the Meiyu-Baiu region and the mid-upper tropospheric cooling in the western portion, we examine the differences in 1000–700-hPa vertical-integrated moisture flux and 700–300-hPa mean horizontal temperature advection between the WIO-LSI and WIO-noLSI cases (Fig. 5). Compared to the WIO-noLSI cases, the WIO cases exhibit stronger moisture convergence within the Meiyu-Baiu region, especially in its eastern portion (shadings in Fig. 5a), which is associated with a cyclonic anomaly of moisture fluxes over the Meiyu-Baiu region and its northern flank (vectors in Fig. 5a). The dynamic component of moisture fluxes and convergence (Fig. 5b), a combination of horizontal wind differences and climatological specific humidity, almost fully replicates the difference between the WIO-LSI and WIO-noLSI cases (Fig. 5a), accounting for more than 70% of the moisture convergence increase averaged over the Meiyu-Baiu region.

The mid–upper tropospheric cooling associated with low SIE under IO warming corresponds well with an enhanced cold advection (Fig. 5c). The cold advection is also primarily caused by wind differences between the WIO-LSI and WIO-noLSI cases, which in turn are largely due to meridional wind differences across the climatological isotherms (Fig. 5d). The wind differences are closely related to the cyclonic anomaly over the Meiyu-Baiu region and its northern flank (vectors in Fig. 5d). This cyclonic anomaly, that dynamically drives lower-level moisture convergence as well as mid-upper level cooling, is part of a quasi-barotropic dipole pattern over East Asia in the geopotential height difference between the WIO-LSI and WIO-noLSI cases (Fig. 6a), with a high pressure anomaly over the East Siberia and a low pressure anomaly on the northern flank of the Meiyu-Baiu region.

To verify the effect of Arctic sea-ice loss on this dipole pattern, we forced Community Atmosphere Model version 6 (CAM6), the atmospheric component of CESM2, with monthly SIC and SST anomalies derived from CESM2LE-simulated WIO-LSI and WIO-noLSI cases (see "Methods" section for details). In their difference (Fig. 6b), we also see robust signatures of the quasi-barotropic dipole pattern over East Asia through the troposphere. The pattern and amplitude of the dipole pattern response in the CAM6 simulations are comparable with the differences between the WIO-LSI and WIO-noLSI cases, although the northern lobe of the dipole pattern is displaced northward especially in the lower troposphere. This suggests that the quasi-barotropic dipole pattern is very likely forced by the sea-ice loss and surface warming along the Eurasian Arctic coast. Despite the damping effect due to the absence of air-sea-ice interaction, the CAM6 results lend support to our interpretation of the atmospheric circulation response to Arctic SST and SIC differences between the WIO-LSI and WIO-noLSI cases.

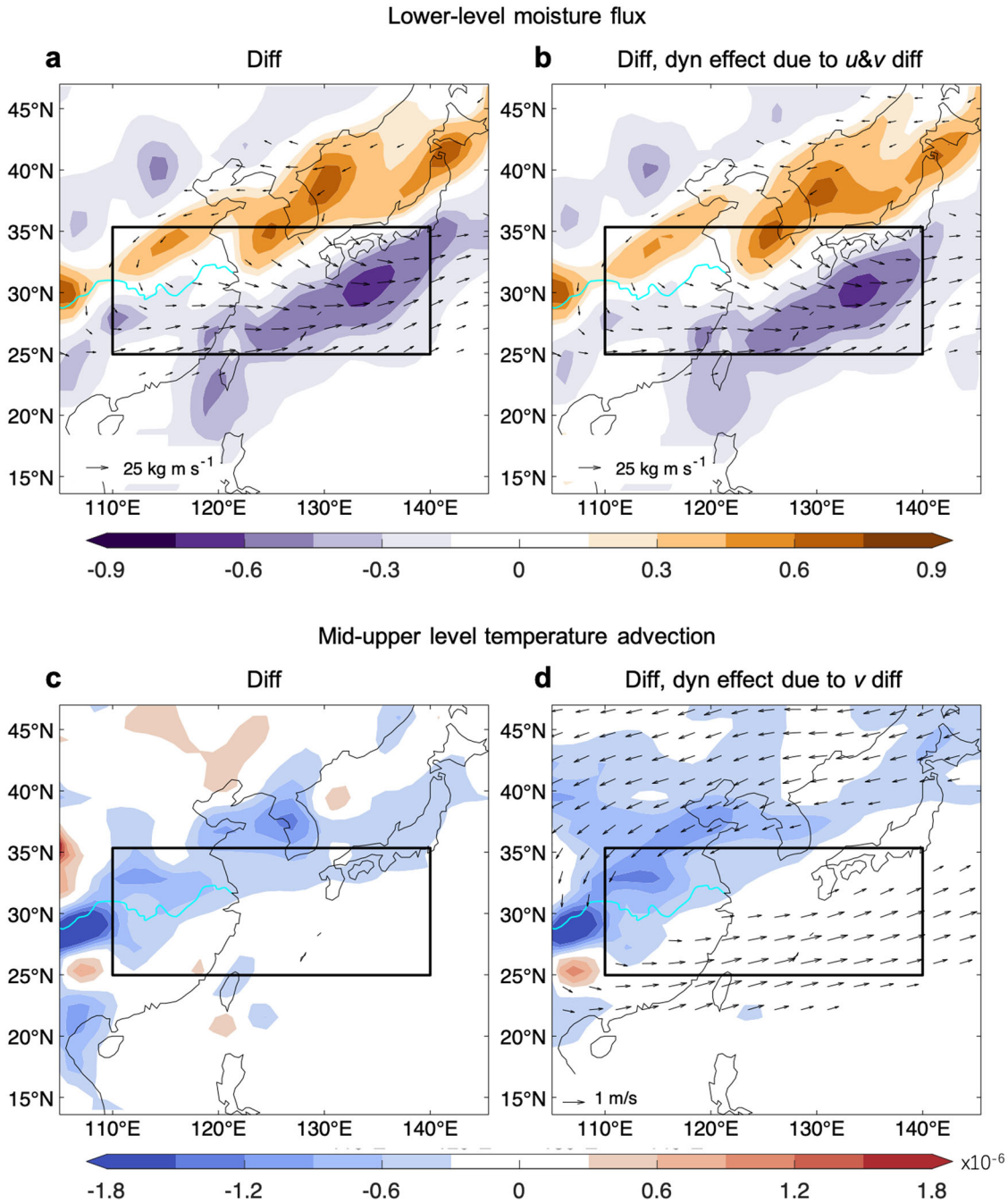

Fig. 5 | Differences in lower-level moisture convergence and mid-upper level temperature advection. a Differences in CESM2LE-simulated vertical-integrated moisture transport from 1000hPa to 700hPa in July between WIO-LSI and WIO-noLSI cases [vectors] and (**b**) its dynamic component due to the horizontal wind differences [vectors], as well as the corresponding moisture flux convergence [shadings]. **c** Differences in CESM2LE-simulated 700-300hPa averaged horizontal temperature advection in July between WIO-LSI and WIO-noLSI cases [shadings] and (**d**) its dynamic component due to the meridional wind differences [shadings]. The vector in panel d shows the 700–300 hPa averaged horizontal winds difference. Only values statistically significant at the 5% level are shown.

It is worth noting that, although a wave train-like pattern across the Eurasian mid-high latitudes is seen in the geopotential height difference in both CESM2LE and CAM6 simulations (Fig. 6), it is almost not statistically significant west of 90°E. Thus, the influence of low KS SIE is largely confined to East Asia. This finding confirms that Arctic sea ice can affect East Asian precipitation through a pathway differing from zonally oriented wave trains such as circumglobal teleconnection and Eurasian teleconnection as previously suggested[20,33,37,38].

Previous studies suggest that the extended ice-free region allows the open ocean to absorb more solar radiation, which then warms the atmosphere by additional turbulence heat flux and long-wave radiation in late spring. The warmed troposphere in the Arctic in turn produces a positive height anomaly over the North Asian in early summer[15,16,22], leading to a strengthened wave train embedded in the polar-front jet and an amplified climatological ridge over East Siberia[15,20]. The enhanced ridge and associated anomalous northeasterlies advect positive vorticity from high latitudes to the northern flank of the Meiyu-Baiu region, leading to a cyclonic (low-pressure) anomaly to the south of the high-pressure anomaly. The CAM6 simulations forced by Arctic SIC anomalies and climatological SST simulate much weaker atmospheric circulation responses (not shown), highlighting the crucial role of Arctic SST warming due to local sea-ice-air feedback in generating atmospheric circulation responses. On the other

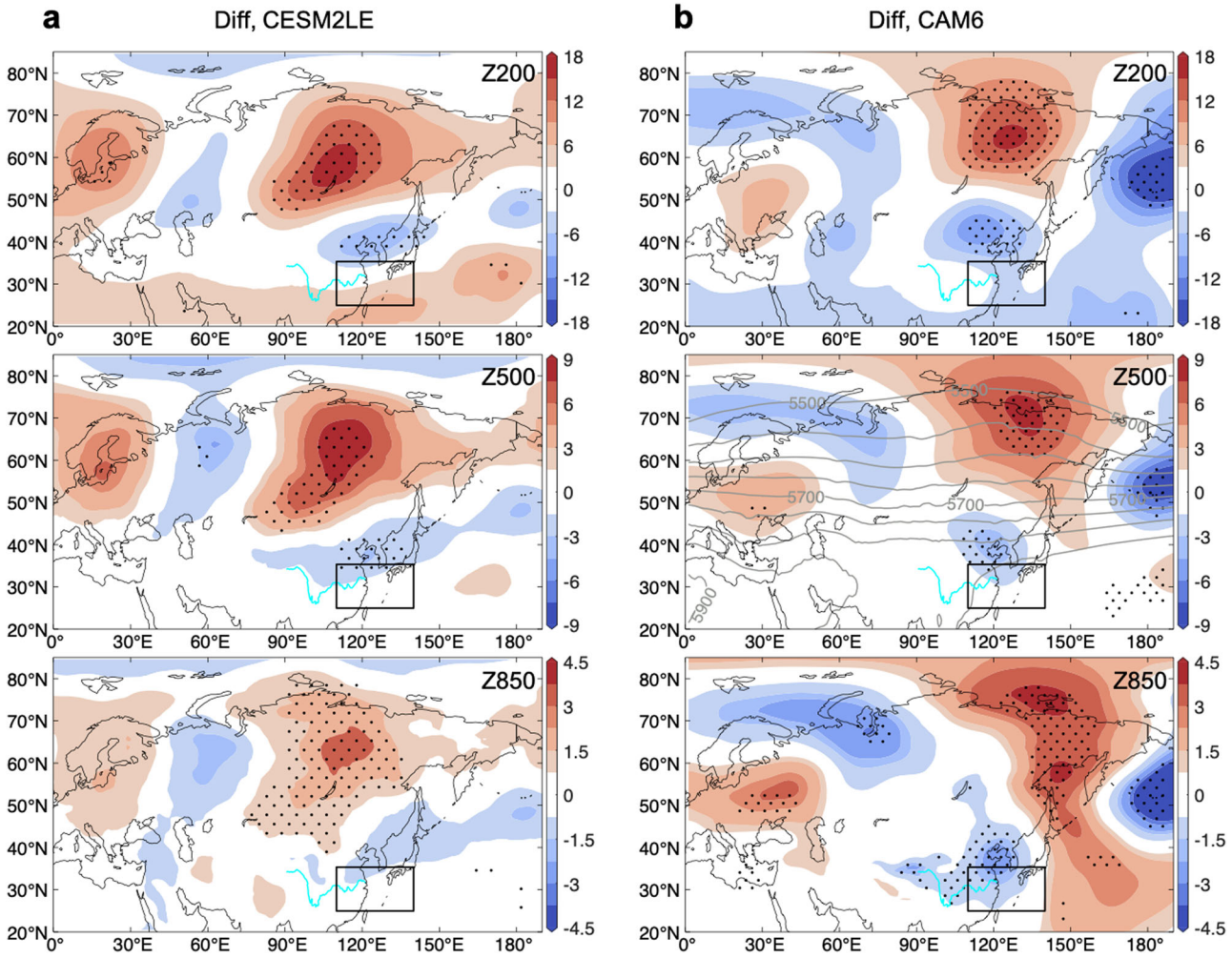

Fig. 6 | Differences in geopotential height. a Differences in CESM2LE-simulated 200-hPa, 500-hPa, and 850-hPa geopotential height [Z200, Z500, and Z850; unit: gpm] in July between WIO-LSI and WIO-noLSI cases. **b** Differences in Z200, Z500, and Z850 in July between atmosphere model (CAM6) experiments (see "Methods" section for details). The stippling represents statistical significance at the 5% level.

hand, the positive height anomaly in eastern Siberia favors atmospheric blocking over North Asia (Fig. S8). This is because Arctic warming and the positive height anomaly along the Eurasian coast weaken the polar front jet and reduce meridional gradients of potential vorticity, favoring long-lived atmospheric blocking events[39,40]. The increased frequency of North Asian blocking also promotes heavy rainfall over the Meiyu-Baiu region[22,41–44].

Improved prediction for July Meiyu-Baiu rainfall

Can the KS SIE improve predictions for the overall variations of July Meiyu-Baiu rainfall and for extremely heavy Meiyu-Baiu cases such as in 2020? Below, we preliminary prove it using a simple statistical prediction model with IO SST, KS SIE, precipitation data from CESM2LE, and observations. Considering the significant linear relationship between IO SST in May and Meiyu-Baiu rainfall in July ($r = 0.31, p < 0.01$) and the asymmetric impact of KS SIE on the Meiyu-Baiu rainfall (with a stronger influence from sea-ice loss than sea-ice increase), we constructed the following statistical model and applied multiple linear regression on all the simulation years from 1950-2014 in CESM2LE (6500 years in total) to estimate the coefficients *b1* and *b2*:

$$Pr = b_1 SST + b_2(e^{-SIE} - 1) + \varepsilon \quad (1)$$

where *SST* and *SIE* represent the standardized timeseries of IO SST and KS SIE in May in CESM2LE, respectively, *Pr* represents the standardized timeseries of precipitation at each grid point in July in CESM2LE, and ε is the residual.

The regression coefficients *b1* and *b2* are broadly positive and statistically significant over the Meiyu-Baiu region (Fig. S9), indicating that the precipitation grows steady with the IO SST increase and grows exponentially with the KS SIE reduction. The regression coefficients are not sensitive to specific ensemble members, but accessing the robust estimates does require a large ensemble of simulations, particularly for *b2* (see Figs. S10 and S11 and Supplementary Notes for details). As shown below, the exponential function used to account for the impact of sea ice in the prediction model significantly improves the prediction for July Meiyu-Baiu rainfall (Fig. 7) compared to other commonly used functions like linear, rational, and sine functions, because it better reflects the stronger influence of low sea ice compared to high sea ice (Fig. S12). On the other hand, it is more objective than the piecewise linear function as it avoids segment choice (Fig. S13).

Then we use the coefficients *b1* and *b2* to predict the observed precipitation:

$$Pr_0 = \left[b_1 SST_0 + b_2(e^{-SIE_0} - 1)\right] \cdot S_0 \quad (2)$$

where *SST0* and *SIE0* are standardized timeseries of observational IO SST and KS SIE, respectively, *S0* denotes the std of observational precipitation timeseries at each grid point, and *Pr0* represents the predicted precipitation at each grid point. This approach is based on the assumption that the relationship among the standardized timeseries of IO SST, KS SIE, and precipitation in the observation is the same as that in CESM2LE, and the

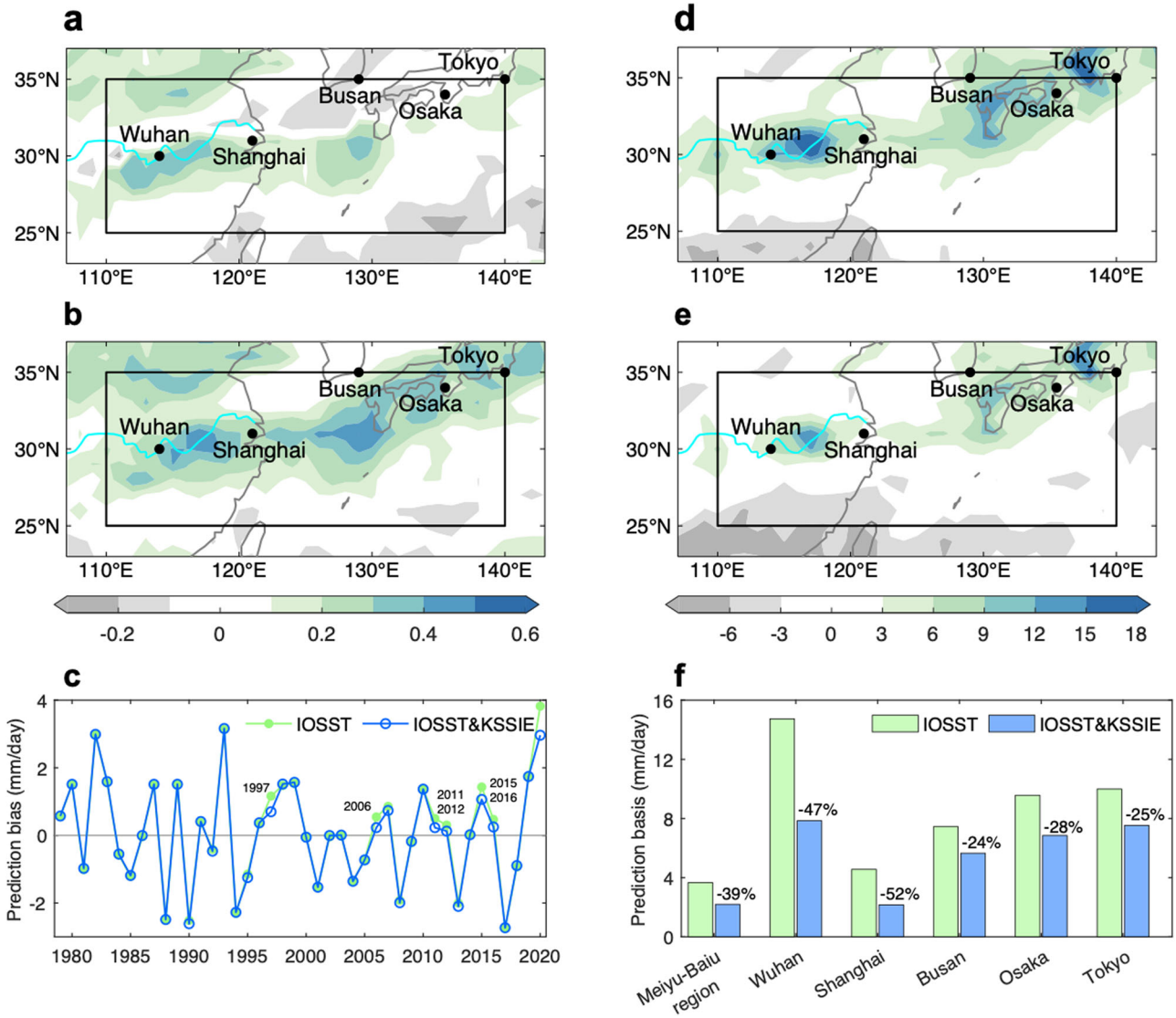

Fig. 7 | Prediction for July precipitation. a, **b** Correlation maps of July precipitation between ERA5 and predictions using (**a**) IOSST and (**b**) IOSST&KSSIE models around the Meiyu-Baiu region during 1950–2020. Black dots highlight five densely populated cities over the Meiyu-Baiu region. **c** Prediction bias [unit: mm/month] averaged over the Meiyu-Baiu region from 1979 to 2020 using IOSST (green) and IOSST&KSSIE (blue) models. **d**–**e** Prediction bias of July 2020 precipitation around the Meiyu-Baiu region based on (**d**) IOSST and (**e**) IOSST&KSSIE models. **f** Differences in July 2020 precipitation between ERA5 and predictions using IOSST (green) and IOSST&KSSIE (blue) models averaged over the Meiyu-Baiu region and around the five cities.

systematic bias in precipitation magnitude can be corrected by the rescaling factor *S0*. This prediction model, called IOSST&KSSIE model, is further compared with another prediction model that solely considers the relationship between IO SST and precipitation, called IOSST model:

$$Pr = b_3 SST + \varepsilon \tag{3}$$

$$Pr_0 = b_3 SST_0 \cdot S_0 \tag{4}$$

Compared to the IOSST model, the IOSST&KSSIE model offers a better prediction skill for the July Meiyu-Baiu rainfall from 1950 to 2020 (Fig. 7a, b). Although the overall improvement is minor and localized along the climatology rain belt (Fig. S1a), the prediction bias is significantly reduced in many years (Fig. 7c). For instance, in 1997, when the spring Arctic sea ice experienced the fastest melting rates in the 20th century[45], the prediction bias for July Meiyu-Baiu rainfall dropped nearly 40%. Similarly, in years with remarkably low sea ice in late spring (e.g., 1997, 2007, 2011, 2012, and 2015), the prediction bias is also notably reduced. While these years do not always coincide with catastrophic Meiyu-Baiu rainfall, they generally coincide with late retreats of Meiyu-Baiu rainfall[3]. Aside from 2020, the prediction for the extremely heavy Meiyu-Baiu rainfall in 2016[11] is also significantly improved. Overall, considering the influence of LSI, the root mean square error (R^2) of prediction from 1996-2020 reduces from 1.09 to 0.91. However, the decrease in R^2 shrinks in a longer period, as the variability of spring Arctic sea ice is relatively small before the mid-1990s[46,47] (Fig. S5c).

Using the IOSST&KSSIE model instead of the IOSST model, the prediction bias of precipitation across the Meiyu-Baiu region in July 2020 is significantly reduced, especially around the middle-to-lower reaches of the Yangtze River (Fig. 7d, e). The bias in the predicted precipitation is reduced by 39% on average over the Meiyu-Baiu region (Fig. 7f). The prediction has also significantly improved for densely populated cities in East China (e.g., Shanghai and Wuhan), southern Japan (e.g., Tokyo and Osaka), and South Korea (e.g., Busan). In particular, the bias is reduced by about 50% for Wuhan and Shanghai, the largest cities in the middle and lower reaches of the Yangtze River, respectively (Fig. 7f).

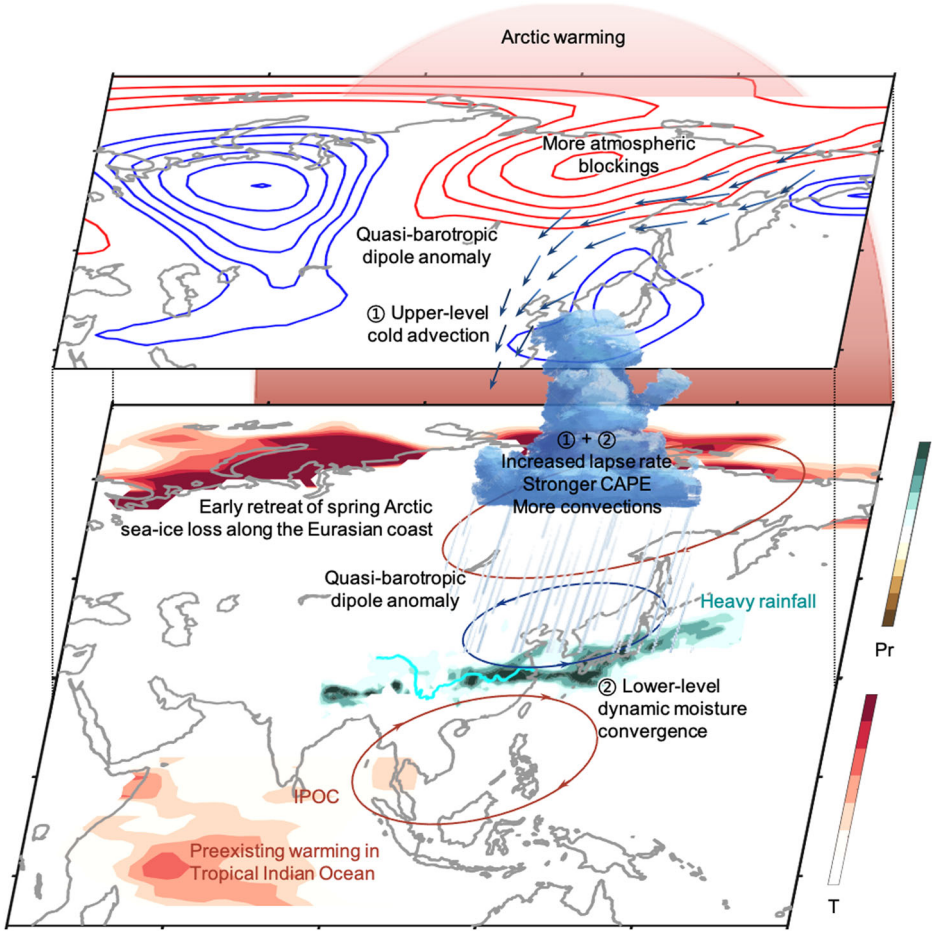

Fig. 8 | Schematic for Arctic sea-ice loss intensifying WIO-induced heavy Meiyu-Baiu rainfall. The physical processes of early retreat of Arctic sea ice along the Eurasian coast in May enhances the Meiyu-Baiu rainfall in the preexisting of WIO.

Discussion

The subseasonal prediction of extremely heavy Meiyu-Baiu rainfall like that in 2020 remains challenging, especially when influences from high latitudes play a role. By analyzing large ensemble simulations, we revealed that low KS SIE in late spring is an important predictor of heavy Meiyu-Baiu rainfall when IO warming occurs. Specifically, we found that in a year with warm IO, the KS sea-ice loss in May can enhance the IO warming-induced heavy Meiyu-Baiu rainfall by ~50%, prolong the Meiyu-Baiu rainy season, and favor extremely heavy rainy days especially around the middle-lower reaches of the Yangtze River, all of which significantly raise the risk of extremely heavy Meiyu-Baiu rainfall. As summarized in Fig. 8, with preexisting IO warming, Arctic warming above the additional ice-free oceans along the Siberian coast can amplify the ridge over North Asia and generate a cyclone anomaly on the north flank of the Meiyu-Baiu region. This cyclonic anomaly, in conjunction with the anomalous anticyclone caused by the Indo-Pacific Ocean Capacitor (IPOC), dynamically converges moisture at lower levels. It also cools the mid-upper troposphere in the western Meiyu-Baiu region, increasing the lapse rate and promoting convective precipitation. These results are echoed by the significantly improved prediction of Meiyu-Baiu rainfall from our newly built statistical model that considers both the preceding IO SST and KS SIE in May. Our findings have important implications for the seasonal prediction of extremely heavy Meiyu-Baiu rainfall, which allows authorities a lead time of one to a couple of months to implement preventive measures and reduce life and property loss.

We note that our quantitative results from CESM2LE may be model dependent. In particular, the coarse resolution of the CESM2LE simulations may hinder an accurate representation of precipitation. For example, the CESM2LE-simulated daily precipitation during Meiyu-Baiu rainfall is more concentrated around the median compared to the observation, suggesting a lack of representation on the days with extremely heavy rainfall. Research on the sensitivity of our results to different models shall further our understanding of the involved physical processes and provide a more precise quantification of the synergistic effect of IO SST and Arctic sea-ice loss on East Asian precipitation, and is desirable in the future.

Although the simple two-parameter statistical prediction model in the current study can to some extent reduces predication bias for July Meiyu-Baiu rainfall and highlight the potential of our findings for predictions, it has significant limitations. For example, the explained proportion of the July Meiyu-Baiu rainfall variance remains small, suggesting the late-spring Arctic sea ice may not be a determined factor. We strongly encourage the use of more sophisticated and comprehensive method in future research to involve the impact of Arctic sea ice in Meiyu-Baiu rainfall predictions, including parametric statistics and mechanic learning methods.

We also note that the prediction lead time for heavy Meiyu-Baiu rainfall jointly caused by low SIE and IO warming is hindered by the poor predictive skill of the summer Arctic SIE (33). Progress in the dynamic prediction of early-summer Arctic sea ice can aid the prediction of catastrophic Meiyu-Baiu rainfall events. We may also take an alternative approach and investigate the causes or precursors of earlier-than-usual Arctic sea-ice retreat along the Eurasian coast in late spring to increase the prediction lead time.

Methods

Observational and reanalysis datasets

Precipitation data from the Global Precipitation Climatology Project (GPCP) version 2.3[48] and ERA5 reanalysis[49] are used. ERA5 precipitation successfully captures the daily evolution of observed Meiyu-Baiu rainfall in June-July 2020[22], suggesting a reasonable representation of super Meiyu-Baiu rainfall. Observations of SST and SIC are from the Hadley Center Sea

Ice and Sea Surface Temperature data set (HadISST)[50]. The regional SIE is defined as the ocean area within the region with at least 15% SIC. We focus on the 1950-2014 period, which has relatively homogeneous and abundant observations and reliable radiative forcing in historical simulations. All anomalies are relative to the 1981-2010 climatology at each calendar day. Area weighting is used in domain averaging.

CESM2LE simulations

We used a 100-member large ensemble of CESM2 (CESM2LE) historical simulations from 1950 to 2014 under CMIP6 historical forcing. These members are initialized from random and different internal atmospheric and oceanic variability but with the same external forcing, despite slightly differences in biomass burning forcing. More details on CESM2LE can be found in Rodgers et al.[27] We used the ensemble-mean timeseries at each grid point to approximate the forced component and obtained the unforced component by removing the forced component in each simulation and at each grid point. CESM2 ranks among the most realistic CMIP6 models for simulating the climatology and interannual variability of the East Asian Summer Monsoon[51,52]. We adopted two-tailed Student's tests to test whether the composite anomalies or differences are statistically significant with a significance level of 5%.

Atmosphere model experiments

We employed the Community Atmosphere Model version 6 (CAM6) for atmosphere model experiments, with a 1.25° lon × 0.9° lat horizontal resolution and 32 vertical levels extending from the surface to 2.26-hPa. The control experiment (CTL) used the 1995–2005 monthly climatological SST and SIC as the lower boundary condition and ran for 75 years, including a 25-year spin-up period. The perturbation experiments, named WIO-LSI-atmos and WIO-noLSI-atmos, are closely mirrored CTL but incorporated SIC and SST anomalies derived from WIO-LSI cases and WIO-noLSI cases in CESM2LE, respectively. The SST and SIC anomalies used in perturbation experiments are shown in Fig. S14. The deviations of WIO-LSI-atmos and WIO-noLSI-atmos experiments from CTL represent the combined effect of WIO and LSI and the isolated effect of WIO alone, respectively. Thus, despite the dampening effect in the atmosphere model simulations due to the absence of air-sea-ice interaction, the difference between WIO-LSI-atmos and WIO-noLSI-atmos experiments can yield qualitative insights into the atmosphere response to the effect of LSI with co-existing WIO.

Definitions of indices

The state of El Niño–Southern Oscillation (ENSO) is measured by the Niño3.4 Index in January, as ENSO is phase-locked onto the boreal winter. Niño3.4 Index is calculated by averaging SSTs in the central-eastern Pacific region (170°W-120°W, 5°S-5°N), which proves most ENSO events well[53].

Atmospheric blocking is identified using a hybrid two-dimensional blocking index[54]. We first calculates the std for the daily Z500 anomalies (relative to daily climatology from 1981-2010) north of 30°N. Any area larger than of $2.5 \times 10^6\,km^2$ consisting of instantaneous Z500 anomalies >1.5 was identified as an instantaneous blocking area. We also requires a reversal of Z500 meridional gradient on the equatorward side of maximum Z500 anomalies within the instantaneous blocking area. A blocked day at a grid point is defined when this point is within the instantaneous blocking area of a blocking. Blocking frequency at each point is calculated in terms of the percentage of blocked days in July.

Decomposing the horizontal moisture convergence and temperature advection

The anomaly of lower-level integrated moisture convergence can be decomposed into three terms[55]:

$$-\frac{1}{g\rho}\langle\nabla_{\mathrm{h}}\cdot(\vec{\mathrm{V}}q)\rangle' = -\frac{1}{g\rho}\langle\nabla_h\cdot(\bar{\vec{V}}q')\rangle - \frac{1}{g\rho}\langle\nabla_h\cdot(\vec{\mathrm{V}}'\bar{q})\rangle - \frac{1}{g\rho}\langle\nabla_h\cdot(\vec{\mathrm{V}}'q')\rangle \quad (5)$$

where q is the specific humidity, $\vec{\mathrm{V}}$ is the horizontal velocity vector, g is the gravity acceleration, and ρ is the water density. The prime denotes the monthly deviation from the climatology, the overbar denotes the climatology, and the angle bracket represents a vertical integration from 1000 hPa to 700 hPa. The terms $(\vec{\mathrm{V}}q)$, $(\bar{\vec{V}}q')$, $\left(\vec{\mathrm{V}}'\bar{q}\right)$, and $\left(\vec{\mathrm{V}}'q'\right)$ represent horizontal moisture flux and its anomalies due to humidity anomalies, horizontal wind anomalies, and nonlinear effect between humidity and wind anomalies, respectively. Thus, the right-hand side terms represent the horizontal moisture convergence anomalies due to thermodynamical, dynamical, and nonlinear effects, respectively.

The anomaly of temperature advection at a pressure level can be broken down into three terms:

$$-(\vec{\mathrm{V}}\cdot\nabla\mathrm{T})' = -\bar{\vec{\mathrm{V}}}'\cdot\nabla\mathrm{T} - \bar{\vec{\mathrm{V}}}\cdot\nabla\mathrm{T}' - \vec{\mathrm{V}}'\cdot\nabla\mathrm{T}' \quad (6)$$

where T is the air temperature and $\vec{\mathrm{V}}$ is the horizontal velocity. The overbar denotes the climatology and the prime denotes the monthly deviation from the climatology. The right-hand side terms represent the anomalous horizonal temperature advection due to the anomalies in horizontal wind, horizontal temperature gradients, and their nonlinear effect, respectively. The anomaly due to wind anomalies can be further divided into the meridional and zonal components: $-v'\cdot\nabla T_y$ and $-u'\cdot\nabla T_x$, where v' and u' represents the meridional and zonal components of wind anomalies.

Data availability

All data are available in the main text or the supplementary. The observational SST and SIC data is obtained from the Met Office Hadley Centre website (https://www.metoffice.gov.uk/hadobs/hadisst/). The observational precipitation data is available on the Global Precipitation Climatology Project (GPCP) website (https://www.ncei.noaa.gov/products/global-precipitation-climatology-project). ERA5 reanalysis datasets are accessible via https://cds.climate.copernicus.eu/cdsapp#!/dataset/reanalysis-era5-pressure-levels-monthly-means?tab=form. CESM2LE simulations are downloaded through the NCAR Climate Data Gateway: https://www.earthsystemgrid.org/dataset/ucar.cgd.cesm2le.output.html. The data are analyzed with MATLAB and CDO (Climate Data Operators). The model simulation data analyzed in this study are available from the corresponding author upon request.

Code availability

The codes of the CAM6 model is available from https://www.cesm.ucar.edu/models/cesm2. The codes used for data processing and visualization are available from the corresponding author upon request.

Received: 22 April 2024; Accepted: 11 September 2024;
Published online: 17 September 2024

References

1. Tao, S.-Y. A review of recent research on the East Asian summer monsoon in China. *Monsoon Meteorol.* 60–92 (1987).
2. Ninomiya, K. & Akiyama, T. Multi-scale features of Baiu, the summer monsoon over Japan and the East Asia. *J. Meteorol. Soc. Jpn. Ser. II* **70**, 467–495 (1992).
3. Ding, Y., Liang, P., Liu, Y. & Zhang, Y. Multiscale Variability of Meiyu and Its Prediction: A New Review. *J. Geophys. Res. Atmos.* **125**, e2019JD031496 (2020).
4. Liang, P., Hu, Z.-Z., Ding, Y. & Qian, Q. The extreme Mei-yu Season in 2020: role of the Madden-Julian oscillation and the cooperative influence of the Pacific and Indian Oceans. *Adv. Atmos. Sci.* **38**, 2040–2054 (2021).
5. NASA. *IMERG measures flooding rainfall from "Plum Rains" in Japan* (2020).
6. Liu, Y., Ke, Z. & Ding, Y. Predictability of East Asian summer monsoon in seasonal climate forecast models. *Int. J. Climatol.* **39**, 5688–5701 (2019).

7. Liang, P. et al. Challenges in predicting and simulating summer rainfall in the eastern China. *Clim. Dyn.* **52**, 2217–2233 (2019).
8. Huang, R. & Wu, Y. The influence of ENSO on the summer climate change in China and its mechanism. *Adv. Atmos. Sci.* **6**, 21–32 (1989).
9. Tanaka, M. Interannual and interdecadal variations of the western North Pacific monsoon and Baiu rainfall and their relationship to the ENSO cycles. *J. Meteorol. Soc. Jpn. Ser. II* **75**, 1109–1123 (1997).
10. Xie, S.-P. et al. Indian Ocean capacitor effect on Indo–western Pacific climate during the summer follOowing El Niño. *J. Clim.* **22**, 730–747 (2009).
11. Zhou, Z.-Q., Xie, S.-P. & Zhang, R. Historic Yangtze flooding of 2020 tied to extreme Indian Ocean conditions. *Proc. Natl Acad. Sci. USA* **118**, e2022255118 (2021).
12. Yan, Y. et al. Subseasonal forecast barrier of the North Atlantic oscillation in S2S models during the extreme mei-yu rainfall event in 2020. *Clim. Dyn.* **58**, 2913–2925 (2022).
13. Bett, P. E. et al. Seasonal rainfall forecasts for the Yangtze River basin of China in summer 2019 from an improved climate service. *J. Meteorol. Res.* **34**, 904–916 (2020).
14. Qiao, S. et al. The longest 2020 Meiyu season over the past 60 years: Subseasonal perspective and its predictions. *Geophys. Res. Lett.* **48**, e2021GL093596 (2021).
15. Coumou, D., Di Capua, G., Vavrus, S., Wang, L. & Wang, S. The influence of Arctic amplification on mid-latitude summer circulation. *Nat. Commun.* **9**, 1–12 (2018).
16. Streffing, J., Semmler, T., Zampieri, L. & Jung, T. Response of Northern Hemisphere weather and climate to Arctic sea ice decline: resolution independence in Polar Amplification Model Intercomparison Project (PAMIP) simulations. *J. Clim.* **34**, 8445–8457 (2021).
17. Zhao, P., Zhang, X., Zhou, X., Ikeda, M. & Yin, Y. The sea ice extent anomaly in the North Pacific and its impact on the East Asian summer monsoon rainfall. *J. Clim.* **17**, 3434–3447 (2004).
18. Guo, D. et al. Mechanism on how the spring Arctic sea ice impacts the East Asian summer monsoon. *Theor. Appl. Climatol.* **115**, 107–119 (2014).
19. Wu, B., Zhang, R., Wang, B. & D'Arrigo, R. On the association between spring Arctic sea ice concentration and Chinese summer rainfall. *Geophys. Res. Lett.* **36**, L09501 (2009).
20. Zhang, P., Wu, Z. & Jin, R. How can the winter North Atlantic Oscillation influence the early summer precipitation in Northeast Asia: effect of the Arctic sea ice. *Clim. Dyn.* **56**, 1989–2005 (2021).
21. Liu, Y. et al. Role of autumn Arctic Sea ice in the subsequent summer precipitation variability over East Asia. *Int. J. Climatol.* **40**, 706–722 (2020).
22. Chen, X., Dai, A., Wen, Z. & Song, Y. Contributions of Arctic sea-ice loss and East Siberian atmospheric blocking to 2020 record-breaking Meiyu-Baiu rainfall. *Geophys. Res. Lett.* **48**, e2021GL092748 (2021).
23. Wang, J., Fu, N., Liang, P. & Li, M. Possible impact of early Spring Arctic Sea Ice on Meiyu Cessation over the Yangtze–Huaihe River Basin. *Atmosphere* **13**, 1293 (2022).
24. Nakamura, T. & Sato, T. A possible linkage of Eurasian heat wave and East Asian heavy rainfall in Relation to the Rapid Arctic warming. *Environ. Res.* **209**, 112881 (2022).
25. Uotila, P., Karpechko, A. Y. & Vihma, T. Links between Arctic sea ice and extreme summer precipitation in China: an alternative view. *Adv. Polar Sci.* **25**, 222–233 (2014).
26. Chen, X., Wen, Z., Song, Y. & Guo, Y. Causes of extreme 2020 Meiyu-Baiu rainfall: a study of combined effect of Indian Ocean and Arctic. *Clim. Dyn.* **59**, 3485–3501 (2022).
27. Rodgers, K. B. et al. Ubiquity of human-induced changes in climate variability. *Earth Syst. Dyn.* **12**, 1393–1411 (2021).
28. Bonan, D. B., Bushuk, M. & Winton, M. A spring barrier for regional predictions of summer Arctic Sea Ice. *Geophys. Res. Lett.* **46**, 5937–5947 (2019).
29. Luo, B. et al. Origins of Barents-Kara sea-ice interannual variability modulated by the Atlantic pathway of El Niño–Southern Oscillation. *Nat. Commun.* **14**, 585 (2023).
30. Xie, S.-P. et al. Indo-western Pacific Ocean capacitor and coherent climate anomalies in post-ENSO summer: a review. *Adv. Atmos. Sci.* **33**, 411–432 (2016).
31. Liu, B., Yan, Y., Zhu, C., Ma, S. & Li, J. Record-breaking Meiyu rainfall around the Yangtze River in 2020 regulated by the subseasonal phase transition of the North Atlantic Oscillation. *Geophys. Res. Lett.* **47**, e2020GL090342 (2020).
32. Li, H., Chen, H., Wang, H., Sun, J. & Ma, J. Can barents Sea Ice decline in spring enhance summer hot drought events over Northeastern China? *J. Clim.* **31**, 4705–4725 (2018).
33. He, S., Gao, Y., Furevik, T., Wang, H. & Li, F. Teleconnection between sea ice in the Barents Sea in June and the Silk Road, Pacific–Japan and East Asian rainfall patterns in August. *Adv. Atmos. Sci.* **35**, 52–64 (2018).
34. DeMott, C. A. & Randall, D. A. Observed variations of tropical convective available potential energy. *J. Geophys. Res.* **109**, D02102 (2004).
35. Murugavel, P., Pawar, S. & Gopalakrishnan, V. Trends of Convective Available Potential Energy over the Indian region and its effect on rainfall. *Int. J. Climatol.* **32**, 1362–1372 (2012).
36. Vallis, G. K. in *Essentials of Atmospheric and Oceanic Dynamics* Ch. 3, 58–61 (Cambridge University Press, 2019).
37. Wu, Z., Li, X., Li, Y. & Li, Y. Potential Influence of Arctic Sea Ice to the Interannual Variations of East Asian Spring Precipitation. *J. Clim.* **29**, 2797–2813 (2016).
38. Wu, B., Zhang, R., D'Arrigo, R. & Su, J. On the relationship between Winter Sea Ice and summer atmospheric circulation over Eurasia. *J. Clim.* **26**, 5523–5536 (2013).
39. Luo, D. et al. Weakened potential vorticity barrier linked to recent winter Arctic sea ice loss and midlatitude cold extremes. *J. Clim.* **32**, 4235–4261 (2019).
40. Luo, D. et al. Arctic amplification-induced intensification of planetary wave modulational instability: A simplified theory of enhanced large-scale waviness. *Q. J. R. Meteorol. Soc.* **n/a**, 1–18 (2024).
41. Chen, Y. & Zhai, P. Two types of typical circulation pattern for persistent extreme precipitation in Central–Eastern China. *Q. J. R. Meteorol. Soc.* **140**, 1467–1478 (2014).
42. Chen, G. T.-J., Wang, C.-C. & Wang, A.-H. A case study of subtropical frontogenesis during a blocking event. *Mon. weather Rev.* **135**, 2588–2609 (2007).
43. Park, Y. J. & Ahn, J. B. Characteristics of atmospheric circulation over East Asia associated with summer blocking. *J. Geophys. Res.: Atmos.* **119**, 726–738 (2014).
44. Wang, Y. Effects of blocking anticyclones in Eurasia in the rainy season (Meiyu/Baiu season). *J. Meteorol. Soc. Jpn. Ser. II* **70**, 929–951 (1992).
45. Zhang, X., Wu, B. & Ding, S. Influence of spring Arctic sea ice melt on Eurasian surface air temperature. *Clim. Dyn.* https://doi.org/10.1007/s00382-022-06267-4 (2022).
46. Chen, D., Gao, Y., Zhang, Y. & Wang, T. Effects of spring Arctic sea ice on summer drought in the middle and high latitudes of Asia. *Atmos. Ocean. Sci. Lett.* **15**, 100138 (2022).
47. Hu, R. et al. Arctic Sea Ice loss inducing Northwest extension of summer precipitation over the Tibetan Plateau. *J. Clim.* **36**, 7865–7877 (2023).
48. Schneider, U. et al. Evaluating the hydrological cycle over land using the newly-corrected precipitation climatology from the Global Precipitation Climatology Centre (GPCC). *Atmosphere* **8**, 52 (2017).
49. Hersbach, H. et al. The ERA5 global reanalysis. *Q. J. R. Meteorol. Soc.* **146**, 1999–2049 (2020).
50. Rayner, N. et al. Global analyses of sea surface temperature, sea ice, and night marine air temperature since the late nineteenth century. *J. Geophys. Res.: Atmos.* **108**, 4407 (2003).

51. Yu, T. et al. Comparisons between CMIP5 and CMIP6 models in simulations of the climatology and interannual variability of the east asian summer monsoon. *Clim. Dyn.* **60**, 2183–2198 (2023).
52. Huang, W. R., Liu, P. Y., Lee, S. Y. & Wu, C. H. Changes in early summer precipitation characteristics over South China and Taiwan: CESM2-LE and CMIP6 multi-model simulations and projections. *J. Geophys. Res.: Atmos.* **127**, e2022JD037181 (2022).
53. Xie, S.-P. *Coupled Atmosphere-Ocean Dynamics: From El Nino to Climate Change* Ch. 9, 211–250 (Elsevier, 2023).
54. Dunn-Sigouin, E., Son, S.-W. & Lin, H. Evaluation of Northern Hemisphere blocking climatology in the Global Environment Multiscale Model. *Mon. Weather Rev.* **141**, 707–727 (2013).
55. Seager, R. & Henderson, N. Diagnostic computation of moisture budgets in the ERA-Interim reanalysis with reference to analysis of CMIP-archived atmospheric model data. *J. Clim.* **26**, 7876–7901 (2013).

Acknowledgements

This study was supported by the National Natural Science Foundation of China (2022YFF0801701). X.C. was supported by National Natural Science Foundation of China (42105017) and China Postdoctoral Science Foundation (BX20200087).

Author contributions

The conceptualization was from X.C. and Z.W.; X.C. conducted the analysis, visualization, and simulations; J.Liu, J.Li, and W.M. contributed significantly to the methodology; R.Z., S.H., and Y.G. contributed significantly to reviewing the paper and interpretating the results.

Competing interests

The authors declare no competing interests.

Additional information

Supplementary information The online version contains supplementary material available at https://doi.org/10.1038/s41612-024-00770-7.

Correspondence and requests for materials should be addressed to Zhiping Wen.